

Lensing of hot spots in Kerr spacetime

An empirical relation for black hole spin estimation

A. I. Yfantis¹, D. C. M. Palumbo^{2,3}, and M. Mościbrodzka¹

¹ Department of Astrophysics / IMAPP, Radboud University, P.O. Box 9010, 6500 GL Nijmegen, The Netherlands
e-mail: a.yfantis@astro.ru.nl

² Center for Astrophysics | Harvard & Smithsonian, 60 Garden Street, Cambridge, MA 02138, USA

³ Black Hole Initiative at Harvard University, 20 Garden Street, Cambridge, MA 02138, USA

Received: April 2025; accepted YY

ABSTRACT

Context. Sagittarius A* (Sgr A*) exhibits frequent flaring activity across the electromagnetic spectrum, often associated with a localized region of strong emission, known as a hot spot.

Aims. We aim to establish an empirical relationship linking key parameters of this phenomenon –emission radius, inclination, and black hole spin– to the observed angle difference between the primary and secondary image (ΔPA) that an interferometric array could resolve.

Methods. Using the numerical radiative transfer code *ipole*, we generated a library of more than 900 models with varying system parameters and computed the position angle difference on the sky between the primary and secondary images of the hot spot.

Results. We find that the average ΔPA over a full period is insensitive to inclination. This result significantly simplifies potential spin measurements which might otherwise have large dependencies on inclination. Additionally, we derive a relation connecting spin to ΔPA , given the period and emission radius of the hot spot, with an accuracy of less than 5° in most cases. Finally, we present a mock observation to showcase the potential of this relation for spin inference.

Conclusions. Our results provide a novel approach for black hole spin measurements using high-resolution observations, such as future movies of Sgr A* obtained with the Event Horizon Telescope, next-generation Event Horizon Telescope, and Black Hole Explorer.

Key words. Black hole physics – Galaxy: center – Gravitational lensing: strong – Methods: numerical – Methods: analytical – Techniques: high angular resolution

1. Introduction

The Event Horizon Telescope (EHT) has produced images of the supermassive black holes Messier 87* (hereafter M87*) and Sagittarius A* (hereafter Sgr A*), providing an unprecedented laboratory for testing accretion models and studying the effects of light propagation in general relativity (GR) (EHTC et al. 2019b, 2022b, 2024b). Additionally, observations by the GRAVITY collaboration have constrained the mass of Sgr A* to $M = 4.3 \times 10^6 M_\odot \pm 0.25\%$ (GRAVITY Collaboration et al. 2022), establishing a crucial reference for event-horizon-scale tests of spacetime, such as black hole spin measurements and potential deviations from GR.

A major obstacle in performing precision spacetime tests from black hole images is disentangling the plasma effects of accretion from the pure GR signatures of the underlying spacetime. The combination of finite observational resolution, strong interstellar scattering along the Galactic Center line of sight, and the short dynamical timescale of Sgr A* (approximately 30 minutes at the innermost stable circular orbit (ISCO) for a Schwarzschild black hole) makes this separation particularly difficult. Consequently, any attempt to estimate the dimensionless spin parameter, $a_* = Jc/GM^2$, must rely on identifying a signature in one of the less plasma-dependent observables.

Among the most distinctive features of black hole spacetimes is their ability to trap photons in unstable yet bound or-

bits (Bardeen et al. 1972). In the case of a Kerr black hole, the shape and size of these orbits depend solely on the black hole’s mass and spin. The region where these bound orbits reside is known as the photon sphere. As photons escape these unstable orbits and reach a distant observer, they appear as a narrow “photon ring” on the image plane, asymptotically approaching the so-called “critical curve”, depending on the number of windings the photon undergoes around the black hole before arrival. These features have been extensively studied in recent works, both theoretically (Cludel et al. 2001; Johannsen & Psaltis 2010; Gralla et al. 2019; Gralla & Lupsasca 2020a; Kocherlakota et al. 2024) and in connection with observations (Johnson et al. 2020; Gralla et al. 2020; Wong 2021). The Black Hole Explorer (BHEX) mission (Johnson et al. 2024; Lupsasca et al. 2024; Galison et al. 2024) has set the precise measurement of the photon ring as a key science goal.

In this work, we focus on a specific effect of BH lensing: the secondary images of localized sources, or “hot spots”, a sub-category of photon rings. Unlike a full ring, the secondary image remains compact and forms a crescent. This provides a unique opportunity to distinguish direct from lensed photons in the image, enabling the application of the mathematical framework developed for null geodesics. We study two key observational effects: the time lag between primary and secondary photons ($n = 0$ and $n = 1$) and the difference in position angle on the screen (ΔPA), with a particular focus on the latter. Specif-

ically, we derive a new analytic approximation for calculating δPA (where δPA denotes the analytic estimate, while ΔPA refers to the observational measurement), propose a method to disentangle the inclination angle (i) from ΔPA measurements, and establish an empirical relation connecting ΔPA to BH spin. This method is entirely achromatic, as it depends solely on the geometric properties of the system rather than specific emission mechanisms. While the appearance of a single hot spot may differ between, e.g. radio and near-infrared wavelengths, the geometric relations underlying our method remain valid in both regimes.

Observations of Sgr A* support the presence of emission from localized regions, as the source exhibits regular flaring events across the electromagnetic spectrum on characteristic timescales of ~ 20 hours. During these events, near-infrared (NIR) radiation can increase by 1–2 orders of magnitude (GRAVITY Collaboration et al. 2020a), while the brightest X-ray flares reach peaks ~ 600 times the quiescent state (Haggard et al. 2019). Additionally, GRAVITY has detected astrometric motion of the Sgr A* brightness centroid and polarimetric signatures associated with flares (GRAVITY Collaboration et al. 2018, 2023). At radio frequencies, observations with the Atacama Large Millimeter/submillimeter Array (ALMA) have linked similar physical effects to corresponding signatures in the light curves of linear polarization (Wielgus et al. 2022a,b; EHTC et al. 2022c). Proposed next-generation improvements to the EHT have specifically targeted improved dynamical imaging sensitivity on the Galactic Center due to the presence of these rapidly evolving events (Doeleman et al. 2023).

Numerous studies have modeled this localized emission (e.g., Broderick & Loeb 2006; Trippe et al. 2007; Hamaus et al. 2009; Tiede et al. 2020; Gelles et al. 2021; Vos et al. 2022; Vincent et al. 2023), and some have sought to connect simulations to observations for model classification (GRAVITY Collaboration et al. 2020b,c; Ball et al. 2021; Aimar et al. 2023; Yfantis et al. 2024a,b; Antonopoulou & Nathanail 2024). As these models increasingly reproduce observational data, a stronger theoretical foundation becomes essential.

The broader concept of hot spots has been linked to physical processes in magnetically arrested disks (MAD; Narayan et al. 2003), which exhibit flux eruption events resembling the flaring activity of Sgr A* (Dexter et al. 2020; Scepi et al. 2022). These events can generate flux tubes—evacuated regions in the accretion flow where electrons become highly accelerated and heated via magnetic reconnection while traveling in strong vertical magnetic fields (Porth et al. 2021; Ripperda et al. 2022). Simulations by Najafi-Ziyazi et al. (2024) suggest that such structures may produce signatures consistent with observations. Another possible explanation is the formation of plasmoids via magnetic reconnection in magnetized disks (e.g., Ripperda et al. 2020; Aimar et al. 2023; Vos et al. 2024). Lastly, an alternative phenomenon that could appear as bright "spots" are the so-called shock waves (appearing as spiral arms) as shown in Conroy et al. (2023). Notably, all these phenomena are theorized to appear with non-Keplerian (typically sub-Keplerian) velocities.

Given the growing scientific progress in both observational and modeling efforts, we anticipate that a direct image or time-resolved movie of a secondary image will become a reality in the near future. In this paper, we present a straightforward and computationally efficient approach to interpreting such observations – contrasting with the full analytic treatment of photon rings – with the goal of constraining BH spin. To this end, we have constructed a library of over 900 models, varying key system pa-

rameters: the spot's orbital radius (r_{hs}), orbital velocity, BH spin (a_*), and inclination angle (i).

In Section 2, we summarize the key mathematical results from previous studies. In Section 3, we present our numerical scheme and the model library we use to study the problem. In Section 4, we introduce our intermediate findings: a simple and highly accurate (sub-degree) approximation for $\delta PA_{0 \rightarrow 1}$, (as opposed to $n \rightarrow \infty$ that is typically considered); along with a simplified formula that has a growing deviation with spin from sub-degree to up to 5° for $a_* = 0.99$. We then show that the mean value of ΔPA over a full orbit of the hot spot is insensitive to i , similar to recent results in Walia et al. (2024). This result favors simple analyses of average deflections, removing the notion of time-dependent orbital phase and the observer's inclination and position angle in downstream fitting. Lastly, we introduce an empirical relation derived from our model library and evaluate its accuracy in reproducing simulation results. We then apply this relation to three sets of mock observations, incorporating reasonable uncertainties for ΔPA , orbital period (P), and r_{hs} . We show that in the general case our method can constrain the BH spin to better than ± 0.3 at 2σ confidence level. In Section 5, we conclude by discussing the implications and potential limitations of this approach for future observations.

2. Mathematical prior

In this subsection we use Boyer-Lindquist coordinates (t, r, θ, ϕ) and natural units, i.e., $G = c = M = 1$, so that both time and distance are measured in [M]. The line element describing the spacetime is

$$ds^2 = -\left(1 - \frac{2r}{\Sigma}\right)dt^2 - \frac{2a_*r \sin^2 \theta}{\Sigma} dt d\phi + \frac{\Sigma}{\Delta} dr^2 + \Sigma d\theta^2 + \left(r^2 + a_*^2 + \frac{2a_*^2 r \sin^2 \theta}{\Sigma}\right) \sin^2 \theta d\phi^2 \quad (1)$$

where a_* is the dimensionless angular momentum per unit mass and

$$\Sigma(r, \theta) = r^2 + a_*^2 \cos^2(\theta), \quad \Delta(r) = r^2 - 2r + a_*^2. \quad (2)$$

We consider a stationary hot spot and show solutions for two quantities: the time lapse (δt) between two subsequent images ($n, n+1$) and the difference in their position angle on the sky (δPA) for an observer at infinity, on the symmetry axis. The solution holds only for $n \rightarrow \infty$, implying that the parameters are evaluated at r_{crit} . For the purpose of this paper we skip the complete solution that contains various steps and different cases, which can be found in numerous papers (e.g. Beckwith & Done 2005; Gralla & Lupsasca 2020b; Wong 2021). Instead we provide the solutions similarly to Gralla & Lupsasca (2020b) as:

$$\delta t = \frac{2}{\sqrt{\tilde{b}^2 - a_*^2}} \left[\tilde{r}_0^2 \left(\frac{\tilde{r}_0 + 3}{\tilde{r}_0 - 1} \right) K \left(\frac{a_*^2}{a_*^2 - \tilde{b}^2} \right) - 2a_*^2 E' \left(\frac{a_*^2}{a_*^2 - \tilde{b}^2} \right) \right] \quad (3)$$

and

$$\delta PA = \pi + \frac{2a_*}{\sqrt{\tilde{b}^2 - a_*^2}} \left(\frac{\tilde{r}_0 + 1}{\tilde{r}_0 - 1} \right) K \left(\frac{a_*^2}{a_*^2 - \tilde{b}^2} \right), \quad (4)$$

where

$$\tilde{r}_0 = 1 + 2\sqrt{1 - \frac{a_*^2}{3}} \cos\left[\frac{1}{3} \arccos\left(\frac{1 - a_*^2}{(1 - \frac{a_*^2}{3})^{3/2}}\right)\right], \quad (5)$$

is the critical radius, denoting the bound photon orbit for the face-on observer ($i = 0^\circ$). The tilde on the rest of the parameters indicates that they are calculated on the critical radius. Then \tilde{b} , the apparent critical curve on an observer's screen in units of M , is given by

$$\tilde{b} = \sqrt{\tilde{r}_0^3 \left[\frac{4\Delta(\tilde{r}_0)}{(\tilde{r}_0 - 1)^2} - \tilde{r}_0 \right] + a_*^2}. \quad (6)$$

Lastly, K and E' , in Equations 3 and 4, represent the first and second complete elliptical integrals respectively, which can be found in math libraries, such as `scipy`.

For the case of a moving hot spot on a circular orbit on the equator there is an extra degree of complexity, since the spot changes position while the photons move to the secondary image, resulting in a necessary correction for δPA (Equation 4)

For the case of a moving hot spot there is an extra degree of complexity, since the spot changes position while the photons move to the secondary image, resulting in a necessary correction for δPA (Equation 4). In the simplest case of a circular orbit on the equator it is given by,

$$\delta PA_{\text{orb}} = \delta PA - \delta t \Omega, \quad (7)$$

where Ω is the angular velocity of the spot.

As stated, these equations describe the problem only for higher-order images ($n \rightarrow \infty$). In this paper however we are interested in the secondary image ($n = 1$), so we need to quantify how much the solution deviates in this case. To our knowledge, there is no published solution for such a case, hence we present it in Section 4.

3. Numerical method

In this section we describe our numerical setup, built inside the general relativistic radiative transfer (GRRT) code `ipole` (Mościbrodzka & Gammie 2018). We have simulated emission from a moving hot spot, closely resembling that implemented in Yfantis et al. (2024a,b). The hot spot lives in circular orbits on the equatorial plane, and it has a Gaussian profile peaking at the center for its key parameters: number density (n_e), electron temperature (Θ_e) and magnetic field strength (B_{field}). Its size is dictated by the number density that has a 1σ radius of $1.5M$ and then a steep cutoff, creating a crisp spot size. While the spot model is defined in BL coordinates, the ray-tracing of photons is done in Kerr-Schild (KS) coordinates. The resolution is set at 256×256 pixels.

Our library consists of models with different values for a variety of parameters (r_{hs} , Ω_{coef} , i , a_*), where r_{hs} is the distance of the spot from the center of the BH and the Ω_{coef} parameter controls the orbital velocity as

$$P = \frac{2\pi}{\Omega_{\text{coef}}} (r_{\text{hs}}^{1.5} + a_*). \quad (8)$$

The Ω_{coef} parameter provides a straight-forward way to simulate sub-Keplerian orbits, highly expected in MADs, or even slower

Table 1. Parameter values in our simulated library.

Parameter	Values
r_{hs}	{4, 5, 6, 7, 8, 9, 10, 11, 12}
Ω_{coef}	{0.25, 0.5, 0.75, 1, 1.25}
i	{0, 10, 20, 25, 30, 60}
a_*	{-0.9, -0.5, 0, 0.5, 0.9}

orbits associated with spiral shock waves. The parameter grid is summarized in Table 1.

During the simulation we record values of the centroids of the two images, and we mask all contributions to light rays from $n > 1$. Given the centroids we define ΔPA as:

$$\Delta PA = \text{atan2}(Y_{\text{cen}_2} X_{\text{cen}} - X_{\text{cen}_2} Y_{\text{cen}}, X_{\text{cen}} X_{\text{cen}_2} + Y_{\text{cen}} Y_{\text{cen}_2}) \quad (9)$$

where X_{cen} , Y_{cen} and X_{cen_2} , Y_{cen_2} refer to the centroid of total intensity of primary and secondary images respectively. It is worth mentioning that the correct ΔPA of a moving source can be estimated only using the slow light approach; otherwise, using the fast light approximation, the second term of Equation 7 cannot be manifested, leading to large deviations¹.

We also measure the arrival time of all photons to the observer, allowing us to calculate the maximum time difference (Δt) between the primary and secondary image as the difference between the first and last photon to reach. In Figure 1, we present two example snapshots from the simulation domain with different parameters, as indicated in the plot title. The middle and right panels display the evolution of ΔPA and Δt over a full orbit. Both quantities exhibit significant variation with increasing inclination, highlighting the need for a method to disentangle inclination effects from other influences. This is presented in the following Section 4.

4. Results

This section includes two intermediate results necessary for the construction of an empirical relation. Those are: 1) an analytic approximation for $\delta PA_{0 \rightarrow 1}$, and 2) the independence of the mean ΔPA (from a full period) from changes in inclination, similarly to the independence of the median value shown in Walia et al. (2024). Table 2 summarizes key parameters of the lensing problem used across the paper. Next we present our empirical relation that covers shortcomings from the analytic relations in order to be used as a means of inference, and lastly we show three examples of its application using mock observations of ΔPA .

4.1. Analytic approximation for $\delta PA_{n \rightarrow 1}$

In order to address this problem we create three models with spin parameters $a_* = 0, 0.5, 0.95$, a smaller spot size (spot radius of $1 M$) and higher resolution (1024×1024 pixels). The spot is stationary and r_{hs} is set to the critical radius for all models.

First we test the simulation results against the δPA solution. While both methods give $\Delta PA = 180^\circ$ for the non-spinning case, for $a_* = 0.5, 0.95$ the analytic solution gives $\delta PA = 216^\circ, 263^\circ$ while the simulations produce $\Delta PA = 198^\circ, 218^\circ$, respectively. The reason is that the trajectories are sufficiently different for $n = 0$ and $n = 1$ that the critical parameters do not apply exactly. Thus the complete integral (K) in Equation 4 should be calculated as incomplete instead (K_{inc}). These are connected via

¹ Note, that ray-tracing of GRMHD snapshots is typically done in fast light (EHTC et al. 2019a, 2022d).

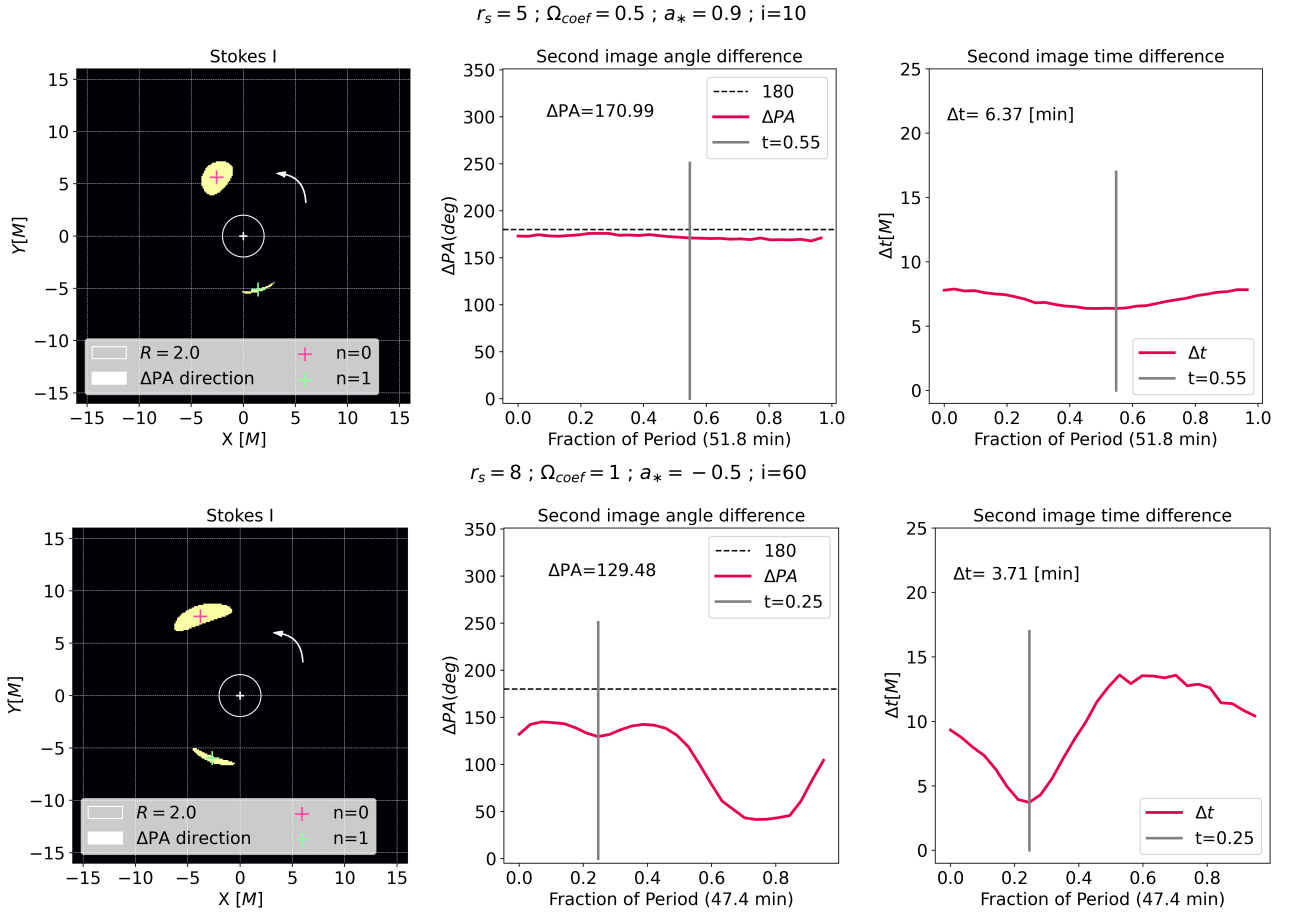


Fig. 1. Left: Snapshot from a hot-spot movie ; middle: the curve of ΔPA measurement during a full period; right: the time lag measurement (arrival time difference) between the first and second image.

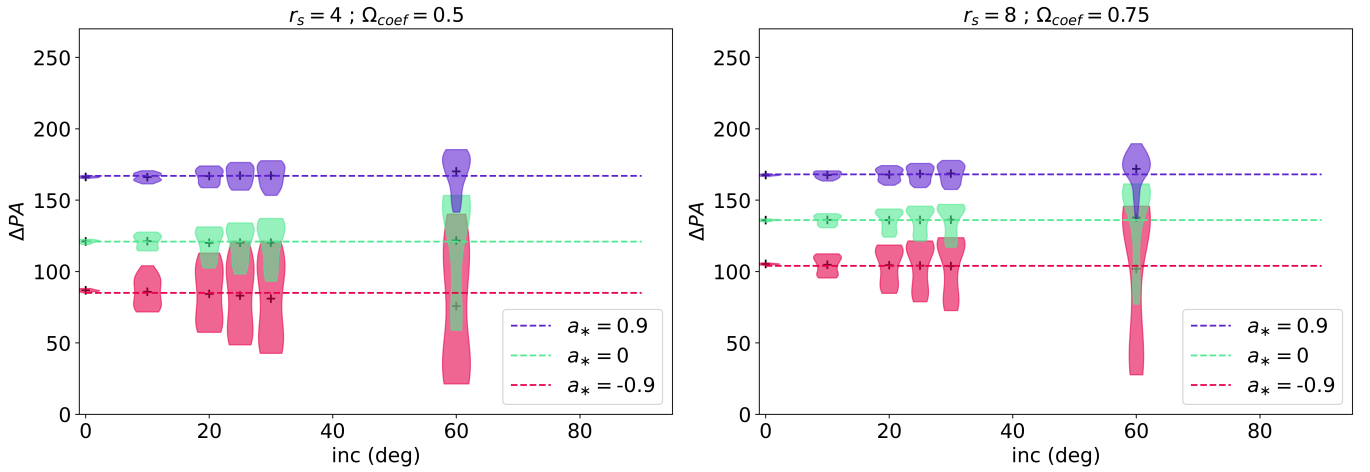


Fig. 2. Distribution (violins) of ΔPA values during a full period for different inclination values. The crosses denote the average values per period and the dashed lines the value at $i = 0^\circ$ for a fixed a_* .

Via trial and error we found that the correct angle for an incomplete integral to account for the primary-secondary ($0 \rightarrow 1$) image solution ($\delta PA_{0 \rightarrow 1}$) is $\pi/(\pi + a_* + 0.3)$ so that

$$K(x) = K_{inc} \left(\frac{\pi}{2} \middle| x \right), \quad (10)$$

where the argument in K_{inc} is an angle in the first part and the calculated quantity in the second. So for $\pi/2$ the incomplete becomes complete.

Table 2. Descriptions of various notations used in the analysis.

Notation	Description
δPA	The analytic solution for angle difference on sky between $n, n+1$ ($n \rightarrow \infty$), for a stationary spot.
$\delta PA_{0 \rightarrow 1}$	The analytic solution for angle difference on sky between $n=0, n=1$ for a stationary spot.
$\delta PA_{f2, 0 \rightarrow 1}$	The analytic approximation (remove “factor 2”) for angle difference on sky between $n=0, n=1$ for a stationary spot.
δPA_{orb}	The analytic solution for angle difference on sky between $n, n+1$ ($n \rightarrow \infty$), accounting for emitter motion.
ΔPA	The observed angle difference on sky between $n=0, n=1$, accounting for emitter motion.
δt	The analytic solution for time difference between $n, n+1$ ($n \rightarrow \infty$).
Δt	The observed time difference between $n=0, n=1$

$$\delta PA_{0 \rightarrow 1} = \pi + \frac{2Ma_*}{\sqrt{\tilde{b}^2 - M^2 a_*^2}} \left(\frac{\tilde{r}_0 + M}{\tilde{r}_0 - M} \right) \times K_{\text{inc}} \left(\frac{\pi}{(\pi + a_* + 0.3)} \middle| \frac{a_*^2}{a_*^2 - \tilde{b}^2} \right). \quad (11)$$

The reason behind the a_* dependency inside K_{inc} is that the deviation of the two formulas (δPA , $\delta PA_{0 \rightarrow 1}$) increases for high spins, as the photons are traveling a larger angle (δPA increases with increasing spin), and that needs to be accounted for. Another effective and significantly simpler way to calculate the deviation in $\delta PA_{0 \rightarrow 1}$ is by taking the expression for δPA (Equation 4) and removing the factor of 2 from the second term. We call this $\delta PA_{f2, 0 \rightarrow 1}$ given as,

$$\delta PA_{f2, 0 \rightarrow 1} = \pi + \frac{a_*}{\sqrt{\tilde{b}^2 - a_*^2}} \left(\frac{\tilde{r}_0 + 1}{\tilde{r}_0 - 1} \right) K \left(\frac{a_*^2}{a_*^2 - \tilde{b}^2} \right). \quad (12)$$

This works nearly exactly (sub-degree deviations) for spins up to ~ 0.75 with deviations of just a couple degrees above that (5° for $a_* = 0.99$). A naive but perhaps useful intuition for this approximation is that the $n=0$ photons do not feel the twist of the spacetime in “their way in”, only as they move towards the back of the BH, and so the deflection between $n=1$ and $n=0$ reflections only half of the effect in the universal regime.

Despite these simplifications, the analytic problem remains challenging due to two key generalizations: the motion of the hot spot and the treatment of a general emission radius r_{hs} , which is not fixed at the critical radius. We therefore proceed with an extensive numerical parameter study to identify a simpler empirical relation.

4.2. Inclination dependence

In order to study the variations of ΔPA with inclination we create distributions (violins) of all ΔPA values, sampled every $dt = 5M$ over a full period, for various models. These are shown in Figure 2, where the models are characterized by two fixed parameter sets ($r_{\text{hs}} = 4, 8$ and $\Omega_{\text{coef}} = 0.5, 0.75$), three spin values ($a_* = -0.9, 0, 0.9$), and five inclination angles in the range $[0, 60]$. The two parameter sets ($r_{\text{hs}}, \Omega_{\text{coef}}$) are shown in separate panels, while all spin values are overlaid within each panel. The vertical axis represents ΔPA , and the horizontal axis denotes the inclination angle.

The distributions shown in Figure 2 exhibit significant variations in both ΔPA values and their shapes depending on the parameters. However, a clear pattern emerges: the mean ΔPA for each model, marked by crosses and connected with dashed lines, remains nearly constant across inclinations. This holds especially well for inclinations up to 30° and for larger values of

r_{hs} . Even in the case of $r_{\text{hs}} = 4$, the deviation at $i = 60^\circ$ from $i = 0^\circ$ is 5° . In the case of Sgr A* inclination is constrained by various observations to be $i \lesssim 30^\circ$ (e.g. GRAVITY Collaboration et al. 2018, 2020b; EHTC et al. 2022d, 2024a; Wielgus et al. 2022b; Levis et al. 2024; Yfantis et al. 2024b,a). Given a full-period dataset, the mean ΔPA can be reliably used for inclination effects. Furthermore, the spread of ΔPA values provides a potential means for estimating inclination itself. This important property enables the creation of a simple empirical relation.

4.3. Empirical relation for ΔPA

We find the following empirical relationship connecting three fundamental parameters of a hot spot around a BH ($r_{\text{hs}}, \Omega_{\text{coef}}, a_*$) with the observed angle difference between primary and secondary image (ΔPA):

$$\Delta PA [^\circ] = 180^\circ + a_*(40 - r_{\text{hs}}) - \left(\frac{1408 - 233a_*}{r_{\text{hs}}^2} + 35 \right) \Omega_{\text{coef}}, \quad (13)$$

where Ω_{coef} , can be expressed in terms of P , r_{hs} and a_* by rearranging Equation 8 (and using physical units) as,

$$\Omega_{\text{coef}} = 2\pi \frac{r_{\text{hs}}^{1.5} + a_*}{P[\text{M}]} = 2.2248 \frac{r_{\text{hs}}^{1.5} + a_*}{P[\text{min}]} \quad (14)$$

where the last expression includes mass of Sgr A* from GRAVITY Collaboration et al. (2022), $M = 4.3 \times 10^6 M_\odot$.

There are three key improvements of Equation 13 with respect to the deflection Equations 11 and 12.

1. The addition of the angular lag caused by the movement of the emitter. This is present in Equation 7, but the complexity increases significantly with the inclusion of δt (Equation 3).
2. The flexibility of r_{hs} , taking all possible values, in contrast to the Equations 11, 12, that are restricted to r_{hs} equal to the critical curve.
3. The simplicity and computational efficiency achieved with Equation 13, since the elliptic integrals E , K are eliminated.

Regarding the individual terms of Equation 13, the second term, $a_*(40 - r_{\text{hs}})$, approximates the angular lag of a stationary emitter. As a single numerical demonstration, we find in a ray-traced hot spot with $a_* = 0.5$ and $r_{\text{hs}} = 2.88$ (the critical radius for this spin) that $\Delta PA = 198.5$, near identical to $\delta PA_{0 \rightarrow 1} = 198$. The next term includes orbital motion through a linear dependence on Ω_{coef} , similarly to δPA_{orb} (Equation 7). The coefficient Ω_{coef} captures variation of both r_{hs} and a_* . We use fitting procedures to find the correct coefficients in Equation 13.

Figure 3 illustrates the performance of this empirical relation. It compares mean ΔPA values (to avoid i dependence) obtained from simulations for a certain set of parameters with those

predicted by Equation 13. The plots have been created to show models with fixed Ω_{coef} ($\Omega_{\text{coef}} = 0.75$ in this case) while varying (r_{hs} and a_*). The bottom panel shows the flat difference between the two ΔPA values, which remains below 5° in all but two cases ($r_{\text{hs}} = 4$, $a_* = -0.5, -0.9$) where it goes up to 10° .

In the following section, we demonstrate its application through explicit examples.

4.4. Mock ΔPA observation

Equation 13 can be solved analytically for a_* , but the resulting expression is cumbersome and impractical to present here. Instead, a more convenient approach is to substitute observed values and solve for a_* . In our case, we employ a Bayesian solver using *dynesty*, a nested sampling tool introduced by [Speagle \(2020\)](#) and further developed by [Koposov et al. \(2023\)](#).

This choice for a Bayesian approach is motivated by two key advantages: 1) it provides a natural framework for incorporating observational uncertainties through Gaussian priors with specified standard deviations, and 2) it yields a posterior distribution for the spin parameter, inherently accounting for measurement uncertainties. By assuming a uniform prior on spin, $a_* \in (-1, 1)$, the resulting posterior directly reflects the inferred constraints on a_* . For the likelihood calculation, we used:

$$\mathcal{L}(\mathbf{p}) = -\frac{[\Delta PA - \hat{\Delta PA}(\mathbf{p})]^2}{2\sigma_{\Delta PA}^2}, \quad (15)$$

where \mathbf{p} is the vector of the model parameters (P , r_{hs} , a_*), ΔPA is the observed value, while $\hat{\Delta PA}$ is the predicted value from our empirical relation in Equation 13. The uncertainty $\sigma_{\Delta PA}$ is taken from observations.

Note that P and r_{hs} are observed with their own uncertainties (σ_P , $\sigma_{r_{\text{hs}}}$) but still re-sampled using their Gaussian distributions as prior (including the full parameter space). This is a similar approach to including all three observables in the \mathcal{L} function and only sampling a_* , but better, because it extracts more information from the system, since the posteriors can have shifted peaks from the mean of the observation. It also provides a more intuitive framework, since it samples 3 values (r_{hs} , P and a_*) and extracts ΔPA that is then compared to the observation.

Given the simplicity of the task, we employ dynamic nested sampling with 1000 live points, one additional batch, and default walker and bound settings. The computation takes approximately one minute on a standard Jupyter notebook running on a typical laptop. The script for this analysis is publicly available at [Github](#)².

We simulate observations in which two bright spots can be identified on the screen, corresponding to the primary and secondary images of a hot spot. In terms of accuracy, the ring diameter was measured as $\hat{d} = 51.9 \pm 2 \mu\text{as}$ in [EHTC et al. \(2022a\)](#). Based on this, we assume a comparable level of accuracy for r_{hs} ($\pm 0.5, M$) and ΔPA ($\pm 5^\circ$). Using these uncertainties, we construct three models, summarized in Table 3. The errors of ΔPA are used for the likelihood calculation of Equation 15, while the errors of the other two parameters are used to define the prior space as a Gaussian distributions.

Before presenting the results, there is a subtle point from our empirical relation (Equation 13) that is worth clarifying. The way we model orbital velocity facilitates comparisons with numerical and analytical disk solutions; however, Ω_{coef} itself is not

directly observable. Instead, observations provide measurements of P and r_{hs} , which can be related to Ω_{coef} and a_* through Equation 8. This implies that we effectively have two equations with two unknowns.

To illustrate this, we present Figure 4, where we use test 1 as a template of observation and perform two different estimations. In the left case, we estimate Ω_{coef} and a_* using two different fits: the “ ΔPA fit,” which relies on our empirical relation (Equation 13), and the “ P fit,” which is based on Equation 8. The “ P fit” constrains Ω_{coef} but leaves a_* completely unconstrained, whereas the “ ΔPA fit” has no direct constraint on Ω_{coef} and only weakly excludes the most extreme spin values.

The bottom-middle panel on the left of Figure 4 shows the two-dimensional posterior distribution of Ω_{coef} and a_* . Although each individual fit allows a_* to span nearly the full prior range, their overlap (highlighted by a black circle) demonstrates how combining both distributions leads to a well-defined solution. This provides a clear validation of our method’s effectiveness.

Instead of using a two-step approach that involves overlapping fits of the two equations, we can incorporate the exploration of Ω_{coef} within a single algorithm, as shown on the right side of Figure 4. In this case, Ω_{coef} is directly obtained from Equation 14 and substituted into the empirical relation. Consequently, it is not treated as a free parameter in the prior and does not appear in the posteriors. Naturally, given the values of r_{hs} , P , and a_* , Ω_{coef} is fully determined. As expected from the previous exercise the spin parameter is nicely constrained at $a_* = -0.16 \pm 0.32$ with 2σ confidence.

The results from tests “2” and “3” are presented in Figure 5. The overall behavior remains consistent with test 1, with one notable difference: the constraining power improves when the spin values are closer to the boundaries. This is evident in the case of $a_* = 0.94^{+0.06}_{-0.18}$, where the uncertainties are less than half those of tests 1 and 3. This behavior is expected, as the true value lies near the boundaries, but it is worth highlighting.

5. Discussion and conclusions

The measurement of a black hole’s spin has occupied astrophysicists for decades, even before the first black hole image from the EHTC ([EHTC et al. 2019b](#)). With upcoming upgrades to the EHTC and ngEHT facilities, advancements in imaging algorithms, and the development of new projects such as BHEx, novel opportunities for spin estimation have emerged (and will continue to do so). This work explores one such avenue, leveraging the interpretation of flaring events around supermassive black holes, particularly Sgr A*, as emission from a well-localized region, a hot spot. This emission is expected to be sufficiently dominant, thus making the secondary image of the hot spot detectable, opening new possibilities for probing the near-horizon spacetime. Among the potential observables, we identify the difference in position angle between the primary ($n = 0$) and secondary ($n = 1$) hot spot images (ΔPA) as a key diagnostic tool.

In this work, we present three key results that facilitate the use of this observable:

1. We derive the correction to the complete elliptical integrals in the analytic relation for δPA , enabling the calculation of $\delta PA_{0 \rightarrow 1}$ in sub-degree accuracy, instead of the commonly used $n \rightarrow \infty$ limit. Additionally, we propose a simplified approximation to the analytic solution that deviates by at most 5° at $a_* \rightarrow 1$ for the same $\delta PA_{0 \rightarrow 1}$ quantity.

² https://github.com/ArYfantis/dyfit_dpa

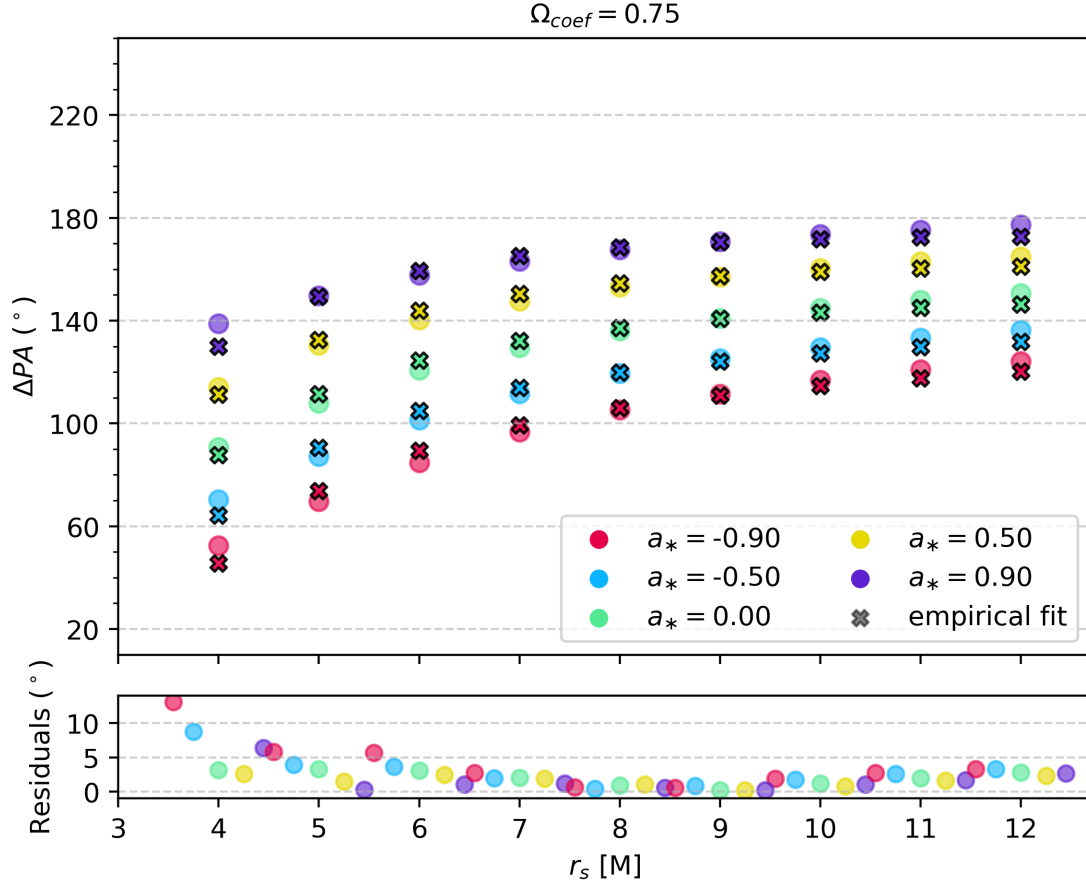


Fig. 3. Mean ΔPA values (from a full period) for different models in our library, overlaid with our empirical fitting relation. The bottom panel shows residuals (percentage difference between ΔPA and $\delta PA_{0 \rightarrow 1}$), where for every radius the spin values have been expanded horizontally for clarity.

Table 3. Mock observation parameters, including a_* from our fits.

Observation Parameters				Spin Estimation		
test	$\Delta PA [^\circ]$	$r [M]$	$P [\text{min}]$	a_*	$2\sigma_{a_*}$	truth
1	140 ± 5	9 ± 0.5	90 ± 3	-0.16	$[-0.48, 0.16]$	-0.18
2	172 ± 5	5.5 ± 0.5	54 ± 3	0.90	$[0.67, 1]$	0.95
3	80 ± 5	4.5 ± 0.5	30 ± 3	-0.71	$[-0.97, -0.36]$	-0.78

Notes. The errors on the observational values are reported as 1σ Gaussian standard deviations. Note that r and P are parameters of the hot spot model, but are also directly constrained in our synthetic observations, so we resample them during fitting with a Gaussian prior given by the measurement.

2. We highlight a distinct effect of orbiting hot spots concerning the system's inclination angle (i). Specifically, when tracking the values of ΔPA over a full orbit of a moving hot spot, we find that the mean value of ΔPA remains unchanged (sub-degree for all cases apart for $r_{\text{hs}} = 4$, $a_* = -0.9$ where deviation is three degrees) for inclinations up to $i \sim 30^\circ$, with deviation of $\sim 5^\circ$ emerging at $i \sim 60^\circ$. This finding significantly simplifies our method, as otherwise, even at $i \sim 25^\circ$ —the expected inclination for Sgr A*—the fluctuations of ΔPA would require a full curve analysis, and thus a more complicated comparison with models.
3. After studying a large library of more than 900 models generated using the GRRT code `ipole`, we achieved our primary goal: constructing a simple empirical relation for estimating spin based on ΔPA observations. This method matches the

analytic solution to within 5° in most cases, with a maximum deviation of 10° for $r_{\text{hs}} \leq 4$ M. To further demonstrate the viability of this method, we conducted three tests, using mock observations with realistic uncertainties, and successfully extracted the spin in all cases, with a maximum uncertainty of ± 0.3 for 2σ confidence.

In the case of an observation that does not capture a full period but for instance 50% of it, we can still yield valuable constraints with a more extensive analysis. One approach is to assume an inclination angle ($i \sim 25^\circ$), and compare the ΔPA curve for several candidate values of the position angle (PA) of the BH spin axis on the sky. This is necessary in order to model the correct phase of the curve. Independent estimates of PA include $PA \sim 130^\circ$ from Ball et al. (2021) and Yfantis et al. (2024a),

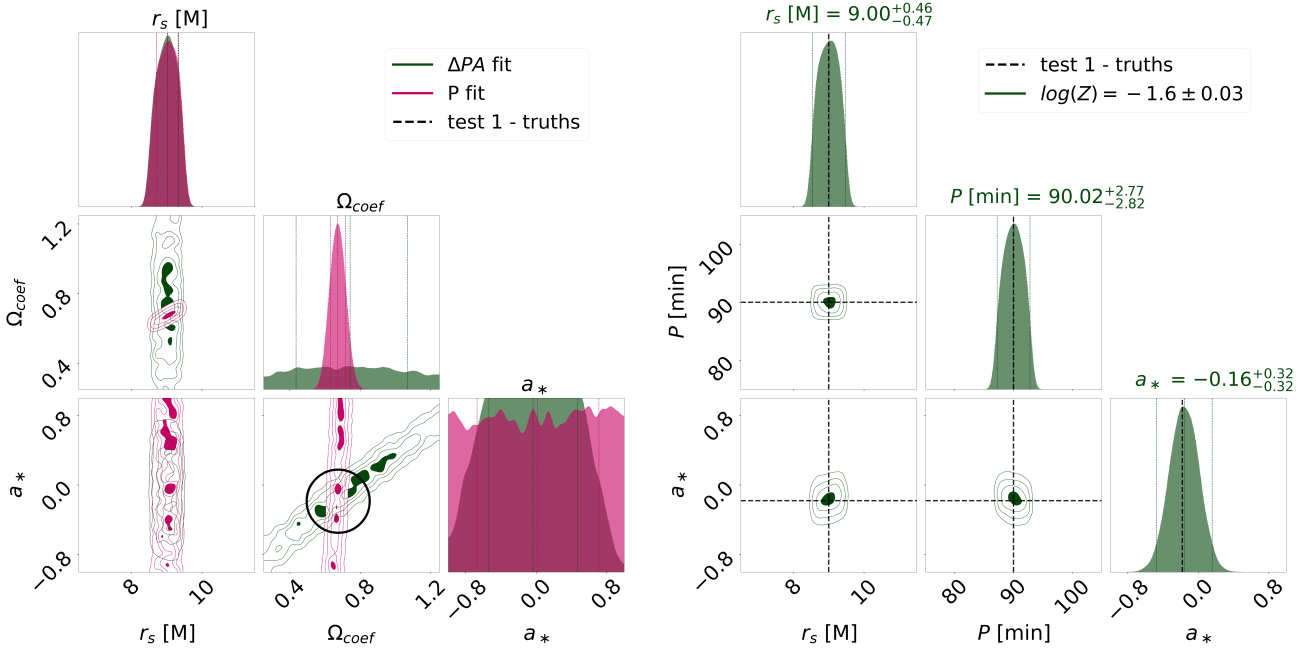


Fig. 4. A Bayesian fit using the mock observations with uncertainties from Table 3, and the empirical relation of Equation 13. Left side shows the fits using Equation 13 and 8 (Period) separately, while right side shows the the fit when combining both.

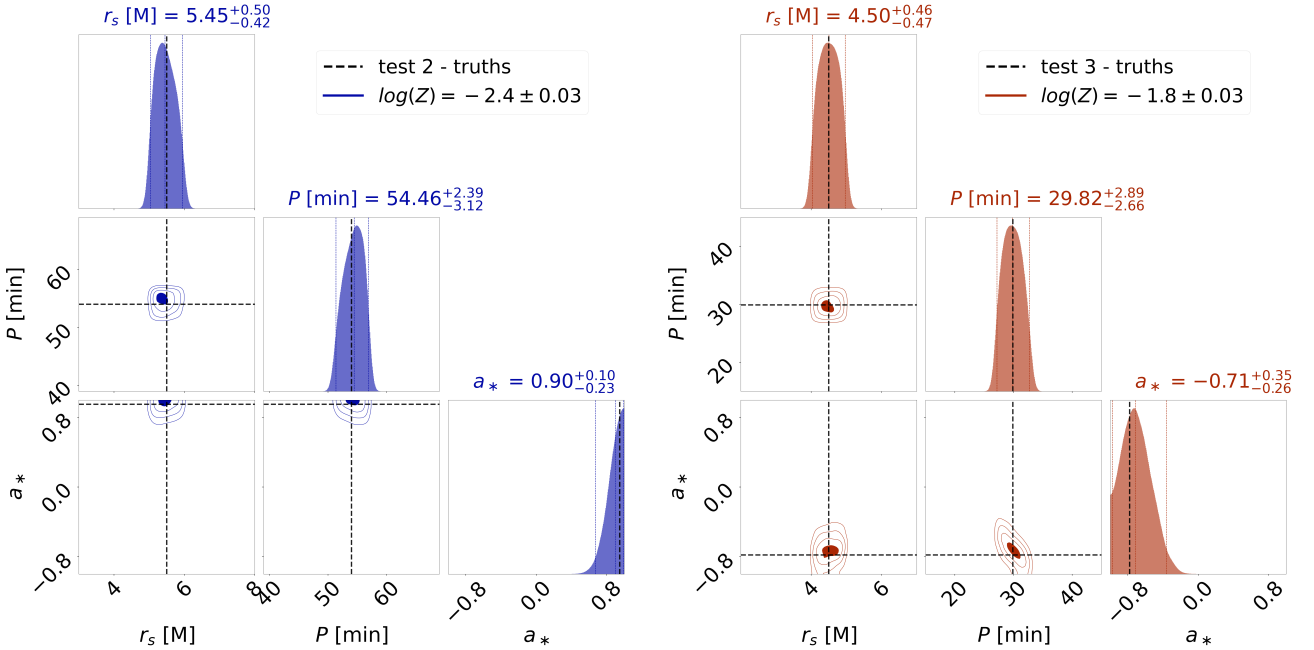


Fig. 5. A Bayesian fit using the mock observations with uncertainties from Table 3, and the empirical relation of Equation 13. Note, that only a_* is the true constrain here, while r_{hs} and P are re-sampled for error propagation.

while Wielgus et al. (2022b); GRAVITY Collaboration et al. (2023); Yfantis et al. (2024b) are consistent with $PA \sim 180^\circ$. From that we could extract the mean ΔPA and continue our moethod. A more robust method would be to create an adaptive Bayesian algorithm utilizing `bipole`, similarly to Yfantis et al. (2024a,b), and explore the full parameter space, jointly fitting for i , PA , r_{hs} , Ω_{coef} and a_* . While this approach requires significantly more computational time (up to ten days, compared to one minute for the current method), it yields a comprehensive posterior over all relevant parameters.

Looking forward, further refinement of this method could focus on expanding the parameter space to include in-falling or out-going orbits; this expansion would more readily reproduce equatorial motions seen in GRMHD. Another interesting addition would be the inclusion of non-equatorial orbits; these could address a big question in the tracking of flaring structures, regarding the mechanism for hot-spot creation, with off-equatorial spots often related to plamsoids rather than flux tubes. Another interesting avenue would be the creation of a machine learning algorithm using an expanded library that treats hot spot observational data more generally, including potentially partial sampling

of the time-dependent astrometry for both images ($n = 0, 1$) and extract all the information for the system (i , r_{hs} , Ω_{coef} , radial velocities, etc.).

Acknowledgements. We thank the anonymous EHT internal reviewer for their comments. This publication is a part of the project Dutch Black Hole Consortium (with project number NWA 1292.19.202) of the research program of the National Science Agenda which is financed by the Dutch Research Council (NWO).

References

- Aimar, N., Dmytriiev, A., Vincent, F. H., et al. 2023, *A&A*, 672, A62
- Antonopoulou, E. & Nathanail, A. 2024, *A&A*, 690, A240
- Ball, D., Özel, F., Christian, P., Chan, C.-K., & Psaltis, D. 2021, *ApJ*, 917, 8
- Bardeen, J. M., Press, W. H., & Teukolsky, S. A. 1972, *ApJ*, 178, 347
- Beckwith, K. & Done, C. 2005, *MNRAS*, 359, 1217
- Broderick, A. E. & Loeb, A. 2006, *MNRAS*, 367, 905
- Claudel, C.-M., Virbhadra, K. S., & Ellis, G. F. R. 2001, *Journal of Mathematical Physics*, 42, 818
- Conroy, N. S., Bauböck, M., Dhruv, V., et al. 2023, *ApJ*, 951, 46
- Dexter, J., Tchekhovskoy, A., Jiménez-Rosales, A., et al. 2020, *MNRAS*, 497, 4999
- Doeleman, S. S., Barrett, J., Blackburn, L., et al. 2023, *Galaxies*, 11, 107
- EHTC, Akiyama, K., Alberdi, A., et al. 2024a, *ApJ*, 964, L26
- EHTC, Akiyama, K., Alberdi, A., et al. 2024b, *A&A*, 681, A79
- EHTC, Akiyama, K., Alberdi, A., et al. 2022a, *ApJ*, 930, L15
- EHTC, Akiyama, K., Alberdi, A., et al. 2019a, *ApJ*, 875, L5
- EHTC, Akiyama, K., Alberdi, A., et al. 2019b, *ApJ*, 875, L1
- EHTC, Akiyama, K., Alberdi, A., Alef, W., et al. 2022b, *ApJ*, 930, L12
- EHTC, Akiyama, K., Alberdi, A., Alef, W., et al. 2022c, *ApJ*, 930, L13
- EHTC, Akiyama, K., Alberdi, A., Alef, W., et al. 2022d, *ApJ*, 930, L16
- Galison, P., Johnson, M. D., Lupsasca, A., Gravely, T., & Berens, R. 2024, *arXiv e-prints*, arXiv:2406.11671
- Gelles, Z., Himwich, E., Johnson, M. D., & Palumbo, D. C. M. 2021, *Phys. Rev. D*, 104, 044060
- Gralla, S. E., Holz, D. E., & Wald, R. M. 2019, *Phys. Rev. D*, 100, 024018
- Gralla, S. E. & Lupsasca, A. 2020a, *Phys. Rev. D*, 101, 044031
- Gralla, S. E. & Lupsasca, A. 2020b, *Phys. Rev. D*, 101, 044031
- Gralla, S. E., Lupsasca, A., & Marrone, D. P. 2020, *Phys. Rev. D*, 102, 124004
- GRAVITY Collaboration, Abuter, R., Aimar, N., et al. 2023, *A&A*, 677, L10
- GRAVITY Collaboration, Abuter, R., Aimar, N., et al. 2022, *A&A*, 657, L12
- GRAVITY Collaboration, Abuter, R., Amorim, A., et al. 2020a, *A&A*, 638, A2
- GRAVITY Collaboration, Abuter, R., Amorim, A., et al. 2018, *A&A*, 618, L10
- GRAVITY Collaboration, Bauböck, M., Dexter, J., et al. 2020b, *A&A*, 635, A143
- GRAVITY Collaboration, Jiménez-Rosales, A., Dexter, J., et al. 2020c, *A&A*, 643, A56
- Haggard, D., Nynka, M., Mon, B., et al. 2019, *ApJ*, 886, 96
- Hamaus, N., Paumard, T., Müller, T., et al. 2009, *ApJ*, 692, 902
- Johannsen, T. & Psaltis, D. 2010, *ApJ*, 718, 446
- Johnson, M. D., Akiyama, K., Baturin, R., et al. 2024, in *Society of Photo-Optical Instrumentation Engineers (SPIE) Conference Series*, Vol. 13092, *Space Telescopes and Instrumentation 2024: Optical, Infrared, and Millimeter Wave*, ed. L. E. Coyle, S. Matsuura, & M. D. Perrin, 130922D
- Johnson, M. D., Lupsasca, A., Strominger, A., et al. 2020, *Science Advances*, 6, eaaz1310
- Kocherlakota, P., Rezzolla, L., Roy, R., & Wielgus, M. 2024, *MNRAS*, 531, 3606
- Koposov, S., Speagle, J., Barbary, K., et al. 2023, *Zenodo*
- Levis, A., Chael, A. A., Bouman, K. L., Wielgus, M., & Srinivasan, P. P. 2024, *Nature Astronomy*, 8, 765
- Lupsasca, A., Cárdenas-Avendaño, A., Palumbo, D. C. M., et al. 2024, *arXiv e-prints*, arXiv:2406.09498
- Mościbrodzka, M. & Gammie, C. F. 2018, *MNRAS*, 475, 43
- Najafi-Ziyazi, M., Davelaar, J., Mizuno, Y., & Porth, O. 2024, *MNRAS*, 531, 3961
- Narayan, R., Igumenshchev, I. V., & Abramowicz, M. A. 2003, *PASJ*, 55, L69
- Porth, O., Mizuno, Y., Younsi, Z., & Fromm, C. M. 2021, *MNRAS*, 502, 2023
- Ripperda, B., Bacchini, F., & Philippov, A. A. 2020, *The Astrophysical Journal*, 900, 100
- Ripperda, B., Liska, M., Chatterjee, K., et al. 2022, *ApJ*, 924, L32
- Scepi, N., Dexter, J., & Begelman, M. C. 2022, *MNRAS*, 511, 3536
- Speagle, J. S. 2020, *MNRAS*, 493, 3132
- Tiede, P., Pu, H.-Y., Broderick, A. E., et al. 2020, *ApJ*, 892, 132
- Trippe, S., Paumard, T., Ott, T., et al. 2007, *MNRAS*, 375, 764
- Vincent, F. H., Wielgus, M., Aimar, N., Paumard, T., & Perrin, G. 2023, *arXiv e-prints*, arXiv:2309.10053
- Vos, J., Mościbrodzka, M. A., & Wielgus, M. 2022, *A&A*, 668, A185
- Vos, J. T., Olivares, H., Cerutti, B., & Mościbrodzka, M. 2024, *MNRAS*, 531, 1554
- Walia, R. K., Kocherlakota, P., Chang, D. O., & Salehi, K. 2024, *arXiv e-prints*, arXiv:2411.15119
- Wielgus, M., Marchili, N., Martí-Vidal, I., et al. 2022a, *ApJ*, 930, L19
- Wielgus, M., Mościbrodzka, M., Vos, J., et al. 2022b, *A&A*, 665, L6, (W22)
- Wong, G. N. 2021, *ApJ*, 909, 217
- Yfantis, A., Wielgus, M., & Mościbrodzka, M. 2024a, *A&A*, 691, A327
- Yfantis, A. I., Mościbrodzka, M. A., Wielgus, M., Vos, J. T., & Jimenez-Rosales, A. 2024b, *A&A*, 685, A142